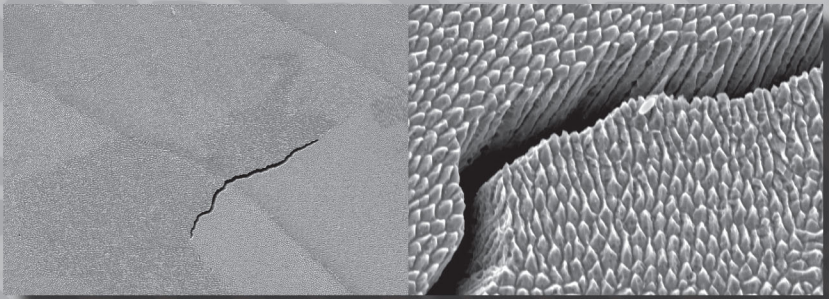


European Conference on  
**Residual Stresses 2018**  
ECRS-10



Edited by  
Marc Seefeldt

M|R|F

# **Residual Stresses 2018**

## **ECRS-10**

10th European Conference on Residual Stresses  
(ECRS10), Leuven, Belgium, 11-14<sup>th</sup> September, 2018.

**Marc Seefeldt**

Chairman ECRS10

KU Leuven, Department of Materials Engineering


Peer review statement

All papers published in this volume of “Materials Research Proceedings” have been peer reviewed. The process of peer review was initiated and overseen by the above proceedings editors. All reviews were conducted by expert referees in accordance to Materials Research Forum LLC high standards.

Cover pictures

The SEM pictures were taken by Maxim Deprez, KU Leuven

Copyright © 2018 by authors

 Content from this work may be used under the terms of the Creative Commons Attribution 3.0 license. Any further distribution of this work must maintain attribution to the author(s) and the title of the work, journal citation and DOI.

Published under License by **Materials Research Forum LLC**  
Millersville, PA 17551, USA

Published as part of the proceedings series

**Materials Research Proceedings**

Volume 6 (2018)

ISSN 2474-3941 (Print)

ISSN 2474-395X (Online)

ISBN 978-1-94529188-3 (Print)

ISBN 978-1-94529189-0 (eBook)

This book contains information obtained from authentic and highly regarded sources. Reasonable efforts have been made to publish reliable data and information, but the author and publisher cannot assume responsibility for the validity of all materials or the consequences of their use. The authors and publishers have attempted to trace the copyright holders of all material reproduced in this publication and apologize to copyright holders if permission to publish in this form has not been obtained. If any copyright material has not been acknowledged please write and let us know so we may rectify in any future reprint.

Distributed worldwide by

**Materials Research Forum LLC**

105 Springdale Lane

Millersville, PA 17551

USA

<http://www.mrforum.com>

Manufactured in the United State of America

10 9 8 7 6 5 4 3 2 1

# Table of Contents

*Preface*

*Committees*

## Diffraction Methods

<b>Single Tilt Method for Residual Stress Evaluation with 2D Detectors</b> B.B. He .....	3
<b>Use of Symmetry for Residual Stress Determination</b> R.C. Wimpory, M. Hofmann.....	9
<b>Neutron Strain Scanning of Duplex Steel Subjected to 4-Point-Bending with Particular Regard to the Strain Free Lattice Parameter <math>D_0</math></b> S. Pulvermacher, J. Gibmeier, J. Saroun, J. Rebelo Kornmeier, F. Vollert, T. Pirling.....	15
<b>Plastic Deformation of InSb Micro-Pillars: A Comparative Study Between Spatially Resolved Laue and Monochromatic X-Ray Micro-Diffraction Maps</b> T. Sadat, M. Verezhak, P. Godard, P.O. Renault, S. Van Petegem, V. Jacques, A. Diaz, D. Grolimund, L. Thilly .....	21
<b><i>In-Situ</i> Analysis of Material Modifications During Deep Rolling by Synchrotron X-Ray Diffraction Experiments</b> H. Meyer, J. Epp.....	27
<b>Residual Stresses Induced in T Butt Welds from Submerged Arc Welding of High Strength Thick Section Steel Members</b> G.W. Sloan, S. Pearceb, V.M. Linton, X. Ficquet, E. Kingston, I. Brown .....	33
<b><i>In-Situ</i> Synchrotron X-Ray Diffraction Studies in the Chip Formation Zone During Orthogonal Metal Cutting</b> J. Gibmeier, D. Kiefer, R. Hofsaess, N. Schell .....	39
<b>Development of Residual Stresses During Laser Cladding</b> A. Narayanan, M. Mostafavi, M. Pavier, M. Peeld.....	45
<b>Round Robin Study on Residual Stresses Using X-Ray Diffraction for Shot-Peened Tool Steel Specimens</b> J. Holmberg, M. Palosaari, S. Hosseini, H. Larjosuo, P. Andersson .....	51
<b>Convergence Behavior in Line Profile Analysis Using Convolutional Multiple Whole- Profile Software</b> M. Kumagai, T. Uchida, K. Murasawa, M. Takamura, Y. Ikeda, H. Suzuki, Y. Otake, T. Hama, S. Suzuki.....	57
<b>High-Resolution Neutron Diffraction Setting for Studies of Macro- and Microstrains in Polycrystalline Materials</b> P. Mikula, M. Rogante, J. Šaroun, M. Vrána .....	63
<b>Stress Measurements of Coarse Grain Materials using Double Exposure Method with Hard Synchrotron X-Rays</b> K. Suzuki, T. Shobu, A. Shiro.....	69

**Study of Error Analysis and Sources of Uncertainty in the Measurement of Residual Stresses by the X-Ray Diffraction**

E.T. Carvalho Filho, J.T.N. Medeiros, L.G. Martinez, V.C. Pinto ..... 75

## **Mechanical Relaxation Methods**

**A Procedure for Plasticity Error Correction for Determination of Residual Stresses by the ESPI-HD Method**

L. Lobanov, F.A.P. Fernandes, V. Savitsky ..... 83

**Hole Drilling Residual Stress Evaluations in Cast Iron**

M. Lundberg, L. Elmquist ..... 89

**Residual Stresses in Railway Axles**

Ř. Bohuslav, V. Jaroslav, N. Tomáš, D. Halabuk ..... 95

**Residual Stress Measurement of the Engineering Plastics by the Hole-Drilling Strain-Gage Method**

A. Kohri, T. Mikami, Y. Suzuki ..... 101

## **Acoustic and Electromagnetic Methods**

**Micromagnetic Analysis of Residual Stress Distribution in 42CrMo4 Steel after Thermal and Mechanical Surface Treatment**

I. Bobrov, J. Epp, H.-W. Zoch ..... 109

## **Composites, Nano and Microstructures**

***In Situ* Mechanical Behavior of Regenerating Rat Calvaria Bones Under Tensile Load via Synchrotron Diffraction Characterization**

A. Zaouali, B. Girault, D. Gloaguen, F. Jordana, M.-J. Moya, P.-A. Dubos, V. Geoffroy, M. Schwartzkopf, T. Snow, H. Gupta, O. Shebanova, K. Schneider, B. Chang ..... 117

## **Films, Coatings and Oxides**

**Residual Stress Analysis in the Oxide Scales Formed on 316L Stainless Steel at 700 °C under Humid Air**

L. Linwei, J. Vincent ..... 125

**Evaluation of Residual Stresses in PVD Coatings by means of Tubular Substrate Length Variation**

H. Lille, A. Ryabchikov, J. Kõo, E. Adoberg, V. Mikli, J. Kübarsepp, P. Peetsalu ..... 131

## **Cold Working and Machining**

**Distinguishing Effect of Buffing Operation on Surface Residual Stress Distribution and Susceptibility of 304L SS and 321 SS Welds to Chloride Induced SCC**

P.S. Kumar, K. Mankari, S.G. Acharyya ..... 139

<b>Comparison of Different Methods of Residual Stress Determination of Cold-Rolled Austenitic-Ferritic, Austenitic and Ferritic Steels</b>	
J. Čapek, K. Trojan, J. Němeček, N. Ganey, K. Kolařík.....	145
<b>Effects of Cutting Parameters on the Residual Stresses of SAE 1045 Steel after Turning</b>	
V.C. Pinto, E.T. de Carvalho Filho, J.T.N. de Medeiros .....	151

## **Heat Treatments and Phase Transformations**

<b>Characterization of Residual Stresses and Retained Austenite on 416 Stainless Steel via X-Ray Diffraction Techniques</b>	
T. Simmons, G. Grodzicki, J. Pineault, J. Taptich, M. Belassel, J. Nantais, M. Brauss .....	159
<b>Comparison of Nondestructive Stress Measurement Techniques for Determination of Residual Stresses in the Heat Treated Steels</b>	
H. Hizli, C.H. Gür .....	165
<b>Evolution of Microstructure and Residual Stress in Hot Rolled Ti-6Al-4V Plates Subjected to Different Heat Treatment Conditions</b>	
W. Rae, S. Rahimi .....	171
<b>Influence of Surface Pretreatment on Residual Stress Field of Heat-Treated Steel Induced by Laser Local Quenching</b>	
Y. Sakaida, Y. Sasaki, H. Owashi .....	177

## **Welding, Fatigue and Fracture**

<b>Residual Stress Formation in Component Related Stress Relief Cracking Tests of a Welded Creep-Resistant Steel</b>	
M. Rhode, A. Kromm, D. Schroepfer, J. Steger, T. Kannengiesser.....	185
<b><i>In-Situ</i> Determination of Critical Welding Stresses During Assembly of Thick-Walled Components made of High-Strength Steel</b>	
D. Schroepfer, A. Kromm, A. Hannemann, T. Kannengiesser .....	191
<b>Reviewing the Influence of Welding Setup on FE-Simulated Welding Residual Stresses</b>	
S. Gkatzogiannis, P. Knoedel, T. Ummenhofer .....	197
<b>Effect of Dengeling on Bending Fatigue Behaviour of Al Alloy 7050 and Comparison with Milling and Shot Peening</b>	
R.L. Peng, L. Selegård, M. Jonsson, M. Ess, G. Petersén.....	203
<b>Analysis of Residual Stress State in Deep-Rolled HT-Bolts</b>	
J. Unglaub, J. Hensel, R. Wimpory, T. Nitschke-Pagel, K. Dilger, K. Thiele.....	209
<b>Comparing the Influence of Residual Stresses in Bearing Fatigue Life at Line and Point Contact</b>	
T. Coors, F. Pape, G. Poll.....	215
<b>Limitations and Recommendations for the Measurement of Residual Stresses in Welded Joints</b>	
T.N. Nitschke-Pagel .....	221

<b>Experimental and Computational Analysis of Residual Stress and Mechanical Hardening in Welded High-Alloy Steels</b>	
N. Hempel, T. Nitschke-Pagel, J. Rebelo-Kornmeier, K. Dilger .....	227
<b>Residual Stress Redistribution During Elastic Shakedown in Fillet Welded Plate</b>	
J.R. Chukkan, G. Wu, M.E. Fitzpatrick, X. Zhang, J. Kelleher .....	233
<b>Modelling the Welding Process of an Orthotropic Steel Deck</b>	
E. Van Puymbroeck, N. Iqbal, H. De Backer .....	239
<b>Strength Calculation of Stiffened Structures Taking Into Consideration Realistic Weld Imperfections</b>	
C. Stapelfeld, B. Launert, H. Pasternak, N. Doynov, V. Michailov .....	245
<b>Contribution to Simplified Residual Stress Calculations of Multi-Layer Welds</b>	
J. Klassen, T. Nitschke-Pagel, K. Dilger .....	251

## **Stresses in Additive Manufacturing**

<b>Residual Stresses in Selective Laser Melted Samples of a Nickel Based Superalloy</b>	
A. Kromm, S. Cabeza, T. Mishurova, N. Nadammal, T. Thiede, G. Bruno .....	259
<b>Evaluation of In-Process Laser Heat Treatment on the Stress Conditions in Laser Metal Deposited Stellite<sup>®</sup> 21</b>	
G.L. Payne, I. Violatos, S. Fitzpatrick, D. Easton, J. Walker .....	265
<b>Residual Stresses Analysis in AISI 316L Processed by Selective Laser Melting (SLM) Treated by Mechanical Post-Processing Treatments</b>	
Q. Portella, M. Chemkhi, D. Retraint .....	271
<b>Analytical Model for Distortion Prediction in Wire + Arc Additive Manufacturing</b>	
J.R. Hönnige, P. Colegrove, S. Williams .....	277
<b>An Analytical Method for Predicting Residual Stress Distribution in Selective Laser Melted/Sintered Alloys</b>	
D. Boruah, X. Zhang, M. Doré .....	283
<b>Determination of the X-Ray Elastic Constants of the Ti-6Al-4V Processed by Powder Bed-Laser Beam Melting</b>	
N. Dumontet, G. Geandier, F. Galliano, B. Viguier, B. Malard .....	289
<i>Keyword and Author Index</i> .....	295
<i>About the Editor</i> .....	301

## Preface

The European Conference on Residual Stresses (ECRS) series is the leading European forum for scientific exchange on internal and residual stresses in materials. It addresses both academic and industrial experts and covers a broad gamut of stress-related topics from instrumentation via experimental and modelling methodology up to stress problems in specific processes such as welding or shot-peening, and their impact on materials properties. After ECRS-8 2010 in Riva del Garda (Italy) and ECRS-9 in Troyes (France), ECRS-10 takes place in Leuven (Belgium). Because of the past and present research activities of KU Leuven and imec on stresses in textured materials, in Microelectronics and Additive Manufacturing, ECRS-10 features the two latter as focus topics, including tutorials for junior researchers. In total, about 170 invited, oral and poster contributions are presented.

Proceedings remain a very valuable source for in-depth reading on the work presented at the conference, and an important reference for the community. After reviewing by two referees each, from the Scientific Committee and/or the Local Organizing Committee, almost 50 contributed papers are included. On behalf of the Organizing Committee, I would like to thank Materials Research Forum and Dr. Thomas Wohlbier for the nice collaboration.

Enjoy reading!

Marc Seefeldt, Chairman ECRS-10



# Committees

## Scientific Committee

- Andrzej Baczmanski, AGH University of Science and Technology, Poland
- Sabine Denis, Institut Jean Lamour, Université de Lorraine, France
- Michael Fitzpatrick, The Open University, United Kingdom
- Manuel François, University of Technology of Troyes, France
- Christoph Genzel, Helmholtz-Zentrum Berlin für Materialien und Energie GmbH, Germany
- Josef Keckes, MU Leoben and Erich Schmid Institute for Materials Science, Austria
- Alexander Korsunsky, University of Oxford, United Kingdom
- Petr Lukáš, Nuclear Physics Institute, Czech Republic
- Eric J. Mittemeijer, MPI for Intelligent Systems and University of Stuttgart, Germany
- João P.S.G. Nobre, University of Coimbra, Portugal and University of Witwatersrand, South Africa
- Ru Lin Peng, Linköping University, Sweden
- Walter Reimers, TU Berlin, Germany
- Paolo Scardi, University of Trento, Italy
- Berthold Scholtes, University of Kassel, Germany
- Marc Seefeldt, KU Leuven, Belgium
- Olivier Thomas, IM2NP, University of Aix-Marseille, France
- Philip Withers, University of Manchester, United Kingdom

## Local Organizing Committee

- Marc Seefeldt, KU Leuven (Chairman)
- Kim Vanmeensel, KU Leuven
- Dimitri Debruyne, KU Leuven
- Barbara Rossi, KU Leuven
- Laurent Delannay, UC Louvain
- Pascal Jacques, UC Louvain
- Thaneshan Sapanathan, UC Louvain
- Ingrid De Wolf, imec and KU Leuven
- Mario Gonzalez, imec
- Maria Strantza, as guest from Los Alamos National Laboratory
- Bey Vrancken, as guest from Lawrence Livermore National Laboratory

# Diffraction Methods



# Single Tilt Method for Residual Stress Evaluation with 2D Detectors

Bob B. He

Bruker AXS Inc, 5465 East Cheryl Parkway, Madison, WI 53711, USA

[bob.he@bruker.com](mailto:bob.he@bruker.com)

**Keywords:** 2D detector, Residual stress, Coating, Thin films, Polymer.

**Abstract.** When X-ray diffraction is used for residual stress measurement, high  $2\theta$  peaks are typically used for enhanced  $2\theta$  shift and better tolerance to the sample height error. But for thin films, coatings, or polymer materials, high  $2\theta$  peaks may not be available or appropriate for stress measurement. As a result of large angular coverage with a 2D detector, residual stress can be measured with a single tilt angle. The diffraction vector coverage from low  $2\theta$  angle diffraction ring can satisfy the stress or stress tensor measurement at a single tilt angle. The single tilt method can avoid the sample height error caused by changing the tilt angle, which is especially critical when measuring stress with a low  $2\theta$  peak. Another advantage is the consistent depth of penetration due to a constant incident angle, which is especially suitable for residual stress measurement on coatings, thin films or samples with steep stress gradient. This paper introduces the single tilt method for stress evaluation with two-dimensional detectors, including experimental examples on coatings and polymers.

## Introduction

Measurement of residual stresses in thin films or coatings by X-ray diffraction is always a challenge due to weak diffraction signals from the thin layer, sharp stress or strain gradients, preferred orientation, anisotropic grain shape and inhomogeneous phase and microstructure distribution [1]. When residual stresses are measured on a coating or thin film sample, it is preferable to keep a small incident angle or control the incident angle to get the most X-ray scattering from the thin film layer. Generally, high  $2\theta$  peaks are preferred for stress measurement due to the more significant  $2\theta$  shift and less sensitive to the sample height error. But for thin films, coatings, or polymer materials, high  $2\theta$  peaks may not be available or appropriate for stress measurement. With low  $2\theta$  peaks, it is more difficult or even impossible to measure stress with the conventional  $\sin^2\psi$  method. With iso-inclination method, the incident angle varies during data collection so the incident angle cannot be kept low during data collection, while with side-inclination method, the actual incident angle to the sample surface is further reduced, and the measurement results become extremely sensitive to the sample height error.

With two-dimensional X-ray diffraction (XRD<sup>2</sup>), stress measurement is based on a direct relationship between stress tensor and diffraction cone distortion [2]. For a diffraction ring with low  $2\theta$ , the diffraction vectors cover more directions at each measurement so that sufficient angular coverage can be achieved with a single tilt. Therefore, the data collection can be done at a fixed  $\psi$  angle with only  $\phi$  rotation. Since the incident angle is constant, the depth of penetration as a function of  $\gamma$  is consistent at all  $\phi$  angles. For most goniometer with Eulerian geometry, the  $\phi$  axis is typically built on precision bearing with very small spherical error, while  $\psi$  rotation is achieved by a circular track which tends to have much more significant spherical error. Avoiding  $\psi$  rotation can significantly reduce the sample height variation during the data collection,

therefore improve the measurement accuracy. As long as the sample height is consistent at various  $\phi$  angles, deviation of the sample surface from the instrument center may affect the pseudo-hydrostatic stress, but has minimal effect on the stress results.

### Geometry and $\Delta\psi$ Coverage

Figure 1 illustrates the diffraction vector distribution for the diffraction pattern collected with a point (0D) detector and a 2D detector. The hemisphere represents all the possible orientations from the origin O of the sample coordinate  $S_1S_2S_3$ . With a point detector, at  $\psi=0^\circ$ , the diffraction vector points to the sample normal direction  $S_3$ . In order to measure stress, the sample has to be tilted at several  $\psi$  angles, for instance  $0^\circ$ ,  $15^\circ$ ,  $30^\circ$  and  $45^\circ$  as indicated by the purple mark  $\otimes$ . With a 2D detector, the trace of the diffraction vector covers a range as shown by the red curve. The diffraction vectors  $H_1$  and  $H_2$  correspond to the two extreme values of  $\gamma_1$  and  $\gamma_2$  on the diffraction ring covered by the 2D detector,  $\Delta\psi$  is the total angular range of the diffraction vector distribution, and  $\Delta\gamma$  is the  $\gamma$  range. At a given tilt angle  $\psi$ , for example  $22.5^\circ$ , the diffraction vector covers a range as shown by the green curve. For low  $2\theta$  diffraction rings at proper detector distance, it is possible to cover sufficient angular range for stress evaluation with a single tilt. The complete data set for stress tensor can be collected at several  $\phi$  angles, for instance  $360^\circ$  scan with  $45^\circ$  steps. Therefore the complete data set are collected with  $\phi$  scan only.

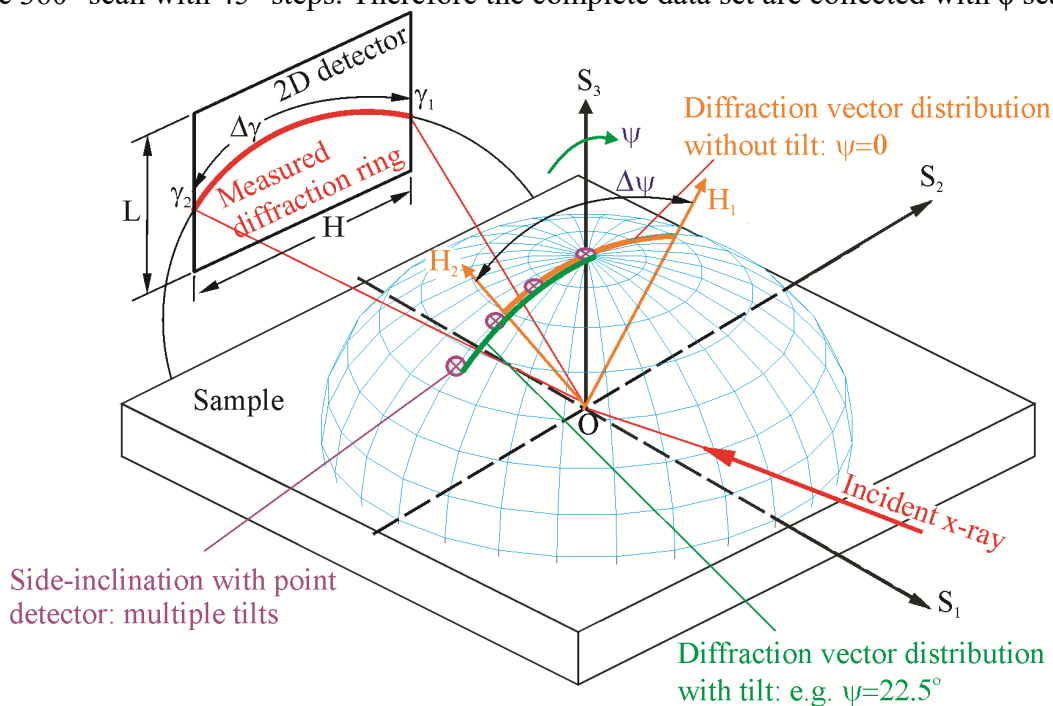


Figure 1. Diffraction vector distribution for 0D and 2D detectors.

The diffraction vector distribution range ( $\Delta\psi$ ) is determined by the detector distance  $D$ , detector height  $H$ , detector width  $L$ ,  $2\theta$  angle and detector swing angle  $\alpha$ . Calculating the  $\Delta\psi$  coverage for a flat detector involves solving some implicit equations [2]. For simplicity, an equation derived from cylindrical detector can be used for  $\Delta\psi$  calculation with negligible error:

$$\Delta\psi = 2 \arcsin\left(\frac{H}{2 \sin \theta \sqrt{4D^2 + H^2}}\right) \quad (1)$$

Here we assume the  $\gamma$  range is limited by the detector height  $H$ . The measured  $\gamma$  range may also be limited by the detector width  $L$  when  $L$  is too small or the detector swing angle is not properly set. Figure 2 shows the diffraction vector distribution range  $\Delta\psi$  as a function of  $2\theta$  calculated for EIGER 2R 500k™ detector at various detector distance and in  $\gamma$ -optimized orientation ( $H=77.2\text{mm}$  and  $L=38.6\text{mm}$ ). For stress measurement with single tilt,  $\Delta\psi$  of more than  $30^\circ$  is acceptable, but the desired  $\Delta\psi$  coverage is  $45^\circ$  or above. A shorter detector distance can be used to increase  $\Delta\psi$ . In general, the angular coverage  $\Delta\psi$  is significantly higher with low  $2\theta$  angles. Therefore, the single tilt method is more suitable for middle or low  $2\theta$  angles.

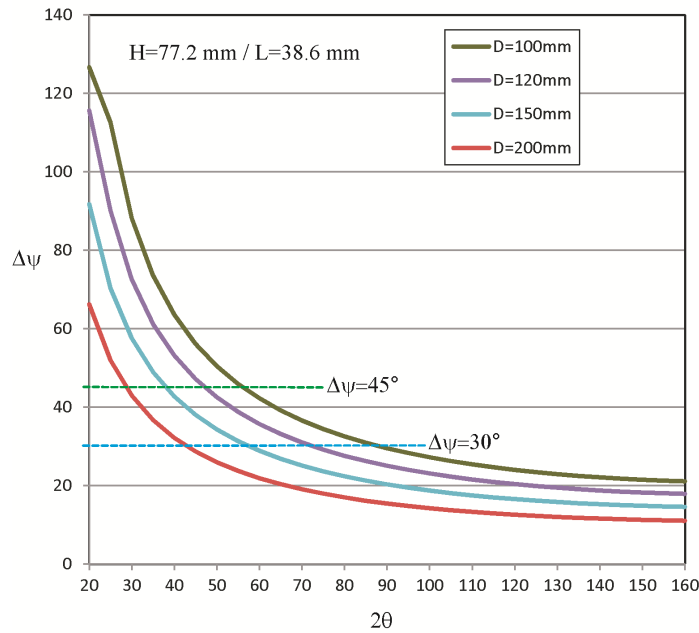


Figure 2.  $\Delta\psi$  range as a function of  $2\theta$  for EIGER 2R 500k™ detector.

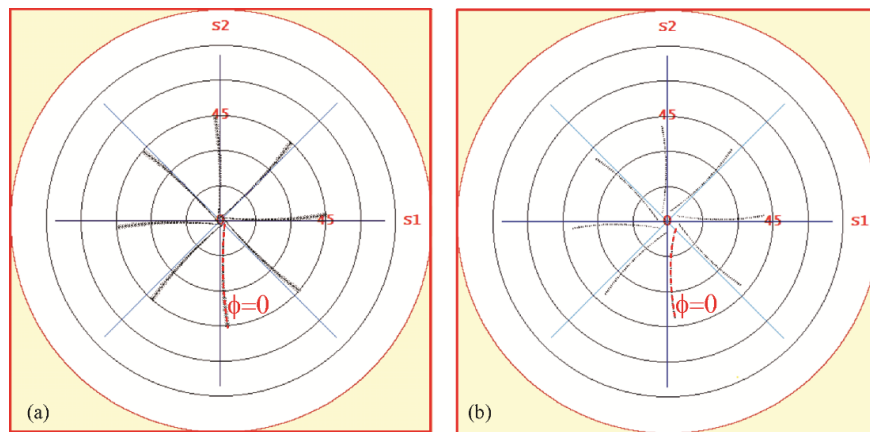


Figure 3. Data collection strategy schemes with single tilt at  $\psi = 22.5^\circ$  and complete  $\phi$  rotation of  $45^\circ$  steps. (a): PE polymer (020),  $2\theta=36.3^\circ$  and  $D=20\text{ cm}$ ; (b):  $\text{Al}_2\text{O}_3(116)$ ,  $2\theta=57.5^\circ$  and  $D=15\text{ cm}$ .

Figure 3 illustrates the single tilt scheme generated with GADDS software for VANTEC-500 2D detector. The left (a) is for PE polymer (020) with  $2\theta=36.3^\circ$ ,  $\psi=22.5^\circ$  and detector to sample

distance  $D=20$  cm and the right (b) is for  $Al_2O_3(116)$  with  $2\theta=57.5^\circ$ ,  $\psi=22.5^\circ$  and  $D=15$  cm. The arcs represent the trace of the diffraction vector corresponding to the data set.  $S_1$  and  $S_2$  are two sample orientations. The red broken curve marks the diffraction vector distribution covered by the frame collected at  $\phi=0$ . With eight frames collected with  $\phi$  scan at  $45^\circ$  steps, the scheme produces comprehensive orientation coverage in a symmetric distribution. The data set collected with this strategy can be used to calculate the complete biaxial stress tensor components.

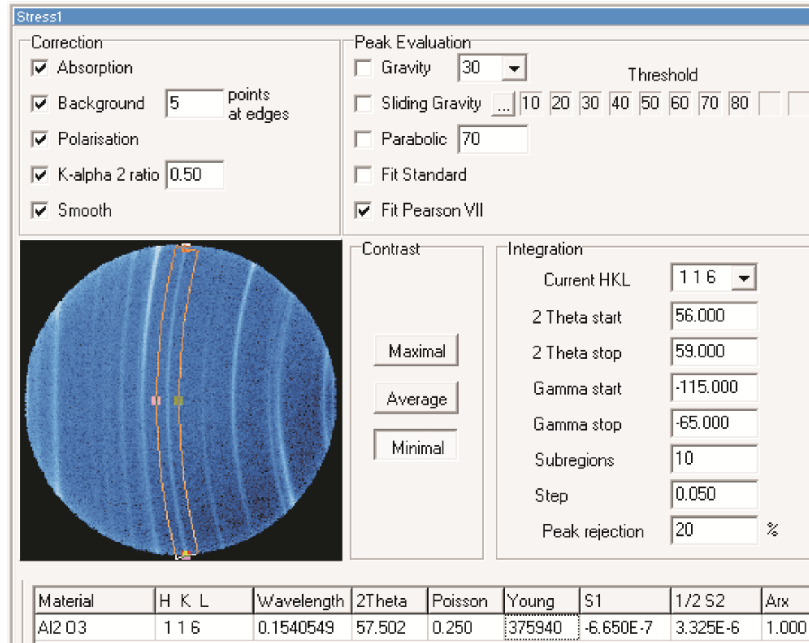


Figure 4. Data evaluation setting for  $1\mu m$  thick  $Al_2O_3$  coating on cutting insert.

The residual stress in the  $Al_2O_3$  coating of less than  $1\mu m$  thick on a proprietary cutting insert is measured with a Bruker D8-DISCOVER system containing centric Eulerian cradle and VANTEC-500 2D detector. With  $Cu-K\alpha$  radiation, the diffraction ring from (116) planes at  $2\theta=57.5^\circ$  is used for stress evaluation. The stress calculation is done with Bruker DIFFRAC.LEPTOS software version 7.9. Figure 4 shows the data evaluation setting. The data integration region is defined by  $2\theta$  range of  $56^\circ$  to  $59^\circ$  and  $\gamma$  range of  $-65^\circ$  to  $-115^\circ$ . The  $50^\circ$   $\gamma$  range is divided into 10 subregions,  $5^\circ$  for each subregion. The counts within each subregion are integrated into a diffraction profile and the  $2\theta$  peak position is determined by one of the five peak evaluation algorithms. In this experiment, Pearson VII function is used to fit the profile and evaluate the  $2\theta$  peak position.

Figure 5 shows the stress evaluation results from one of the data set. The charts above “A” are the fitted data points on 2D frames. The charts above “B” are fitted data points in  $\gamma$ - $2\theta$  rectangular coordinates with magnified  $2\theta$  scale, in which, black line indicates  $2\theta_0$ , blue cross and line indicates the data points from the profile fitting of each subregion, and red line represents the calculated diffraction rings from the stress results. The scattering of the crosses about the red line represents the quality of the data, affecting the standard deviation of the stress results. Any roll error of the detector will change the trend of the fitted data points and the red line, thus the stress results. By click on any data point, the integrated profile displays above “C”. With 60 seconds per frames, the total data collection time is 8 minutes. The measured stress

values are given in the region “D” as  $\sigma_{11}=954.7\text{MPa}$ ,  $\sigma_{22}=957.9\text{MPa}$  and standard deviation  $26.5\text{MPa}$  (<3%).

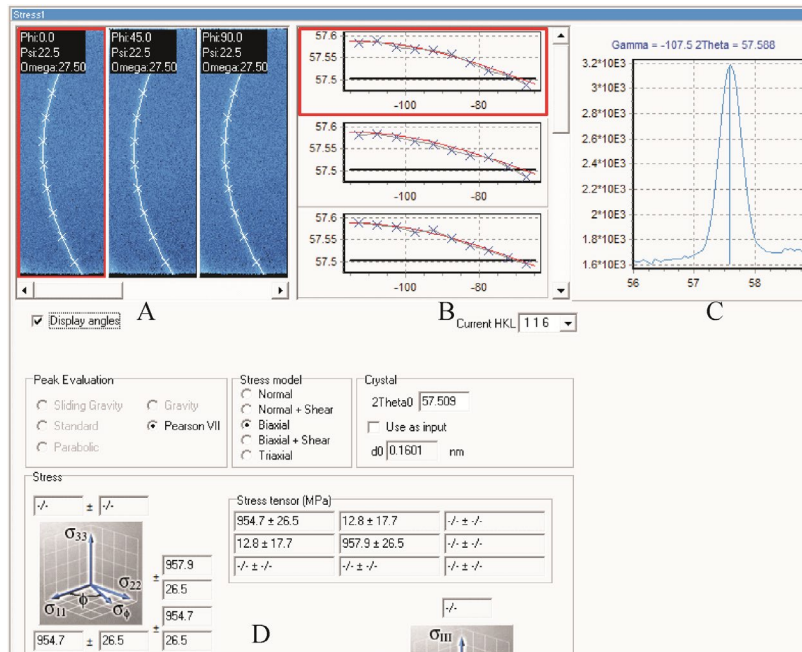


Figure 5. Data evaluation results for  $1\ \mu\text{m}$  thick  $\text{Al}_2\text{O}_3$  coating on cutting insert.

The single tilt stress measurement method is especially suitable for measuring residual or loading stresses in polymers. For stress measurement by X-ray diffraction, the polymer sample must contain sufficient crystalline phase. The crystalline peaks from polymers are typically with low  $2\theta$  angles. For instance, polyethylene (PE) polymer contains mainly three diffraction rings at  $2\theta$  about  $21.4^\circ$ ,  $23.6^\circ$  and  $36.3^\circ$  with Cu-K $\alpha$  radiation, corresponding to crystalline planes of (110), (200) and (020) respectively. Even with the  $36.3^\circ$  peak, a large error in stress result can be introduced by the sphere of confusion with multiple sample tilt angles. The single tilt method can overcome this problem. Other challenge for stress measurement on polymers is the low stress value. However, due to the extremely low Young’s modulus, such as 1070 MPa for high density polyethylene, the  $2\theta$  shift (strain) is also more significant for the same stress if compared with metals. Due to large depth of penetration, the zero normal stress assumption ( $\sigma_{33}=0$  on sample surface) for polymers may not be as accurate as for metals.

Residual stresses on a high-density polyethylene (HDPE) pipe are measured with the single tilt method [3]. An XRD<sup>2</sup> system in vertical  $\theta$ - $\theta$  configuration (Bruker D8-DISCOVER™) with I $\mu$ S™ Cu microsource and VANTEC-500™ 2D detector is used for the measurement. The HDPE pipe has a diameter of 32 mm and wall thickness of 3 mm. The length of the sample is 50 mm, cut from a pipe. Residual stresses of a total 7 points in the outer surface of the pipe and along the axial direction were measured. The depth of penetration corresponding to 50% of the total diffracted intensity is 0.3 mm estimated from the diffraction condition in diffractometer plane ( $\gamma=-90^\circ$ ). To avoid relaxation effect near the cutting edges, the measurement starts at 10 mm from one end with 5 mm steps and completes at the last point 10 mm from the other end. A total of 8 frames are collected for each measurement point with the data collection strategy given in Figure 3(b). Figure 6 shows the data evaluation setting and fitting results with LEPTOS software for one of the measurement point. The measured stresses are tensile in the pipe



extrusion direction with variation of 1.3~2.2 MPa over the 7 points, and compressive in the hoop direction with variation of 6.5~8.1 MPa.

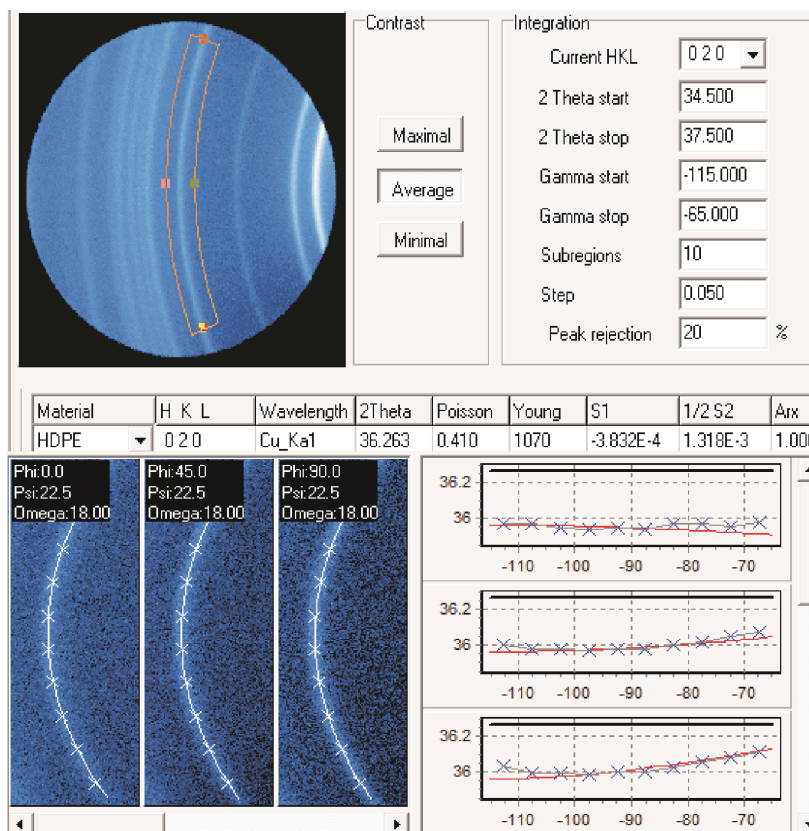


Figure 6. Data evaluation setting and fitting results for the HDPE pipe.

### Summary

For thin films, coatings, or polymers, when the diffraction peaks at high  $2\theta$  angles are not available or appropriate, a low  $2\theta$  peak may be used for stress evaluation. With diffraction rings at low  $2\theta$  angle, the diffraction vector distribution can satisfy the angular coverage for stress or stress tensor measurement at a fixed tilt angle ( $\psi$ ). Without  $\psi$  change during data collection and with  $\phi$  rotation only, the sample height is accurately maintained and data collection time is reduced. The single tilt method is a unique method only achievable with an XRD<sup>2</sup> system, which can measure residual stress with high accuracy and high speed for thin films, coatings and polymers with low to medium  $2\theta$  peaks.

### References

- [1] B. B. He, Measurement of residual stresses in thin films by two-dimensional XRD, Materials Science Forum, Vols. 524-525, (2006) 613-618.  
<https://doi.org/10.4028/www.scientific.net/MSF.524-525.613>
- [2] B. B. He, Two-dimensional X-ray Diffraction, 2<sup>nd</sup> ed., John Wiley & Sons, 2018.  
<https://doi.org/10.1002/9781119356080>
- [3] M. Ren, C. Zheng, Y. Shi, Y. Tang, B. He, Residual stress measurement of high-density polyethylene pipe with two-dimensional X-ray diffraction, Adv. X-ray Anal. 61 (2018).

## Use of Symmetry for Residual Stress Determination

Robert Charles Wimpory<sup>1,a\*</sup> and Michael Hofmann<sup>2,b</sup>

<sup>1</sup> Helmholtz Centre Berlin for Materials and Energy, Hahn-Meitner-Platz 1, 14109 Berlin, Germany

<sup>2</sup> Heinz Maier-Leibnitz Zentrum (MLZ), Technische Universität München, Lichtenbergstr. 1, 85748 Garching, Germany

<sup>a</sup>robert.wimpory@helmholtz-berlin.de, <sup>b</sup>Michael.Hofmann@frm2.tum.de

**Keywords:** Surface Effect, Absorption Effect, Neutron Diffraction, Aberrations, Round Robin, Standardization, Grain Size Effects, Plane Stress Calculations, Nickel Alloy

**Abstract.** Instrumental and certain sample characteristics can affect the detected Bragg peak shifts which are not related to the strain being measured. Three major effects can influence the measurement: the surface effect, where the instrumental gauge volume (IGV) is not fully immersed at a surface or interface, the grain size effect where there is random positioning of large grains in the sample within the gauge volume and the relative shift in position of the centre of gravity of measurement due to absorption of neutrons. All of these effects can be reduced/eliminated by making pairs of neutron diffraction measurements 180 degrees to each other at the same location. Results are presented from a round robin benchmark weldment, denoted TG6, from the European Network on Neutron Techniques Standardization for Structural Integrity (NeT). This is made from a nickel alloy which has large grains and strains and has a high neutron attenuation coefficient.

### Introduction

The surface effect, where the instrumental gauge volume (IGV) is not fully immersed at a surface or interface, normally results in a detected shift of the Bragg-peak and is not related to strain. Webster et al [1] noticed that the instrumental surface effect is essentially symmetrical. This aberration is influenced by a number of parameters, such as the bending radius when using a perfectly bent monochromator [2, 3] and is therefore instrument specific. Figure 1 shows the surface effect when measuring with a  $2 \times 2 \times 10 \text{ mm}^3$  gauge volume on E3 at the HZB [4] (where 10 mm is the gauge volume height) on a nominally strain-free 10mm thick ferritic steel sample. Making pairs of measurements  $180^\circ$  to each other show the symmetrical nature of the surface effect. The bending radius of the Si [400] monochromator is set fortuitously so the surface effect is almost canceled out for the out-of-plane normal direction for this particular  $2\theta$  scattering angle. Averaging the pairs of measurements for each corresponding position results in values that are consistent from the surface to the inside of the specimen (see table 1). Holden et al [5] found that for large-grained samples making pairs of neutron diffraction measurements  $180^\circ$  to each other is a way of minimizing the scatter coming from the random positioning of grains within the gauge volume. Also the relative shift in position of the centre of gravity of measurement due to absorption of neutrons [6] can be cancelled out using this  $180^\circ$  technique. The following results presented are from a round robin benchmark weldment, denoted TG6, from the European Network on Neutron Techniques Standardization for Structural Integrity (NeT). This is made from a nickel alloy which has large grains, large strains and a high neutron attenuation coefficient, making it ideal for testing out the ‘ $180^\circ$ ’ technique.



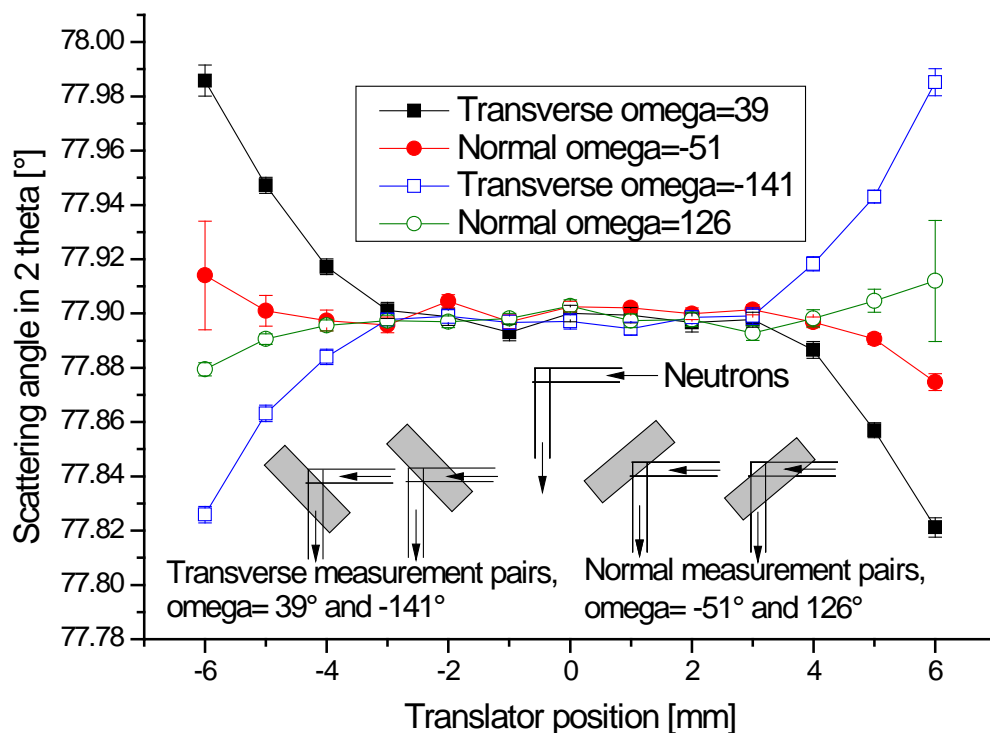


Figure 1. The surface effect of in-plane (transverse) and out of plane (normal) direction on E3.

Table 1. Measurement on a nominally strain-free 10mm thick ferritic steel sample.

Translator position [mm]	Actual position [mm]	Transverse $\omega=39$ [°]	Normal $\omega=-51$ [°]	Transverse $\omega=-141$ [°]	Normal $\omega=126$ [°]	Transverse Average [°]	Normal Average [°]
-6.00	-4.86	77.9858	77.9140	77.8259	77.8794	77.9059	77.8967
-5.00	-4.51	77.9472	77.9010	77.8632	77.8906	77.9052	77.8958
-4.00	-3.88	77.9172	77.8974	77.8840	77.8956	77.9006	77.8965
-3.00	-3.00	77.9011	77.8958	77.8978	77.8974	77.8995	77.8966
-2.00	-2.00	77.8988	77.9045	77.8990	77.8970	77.8989	77.9008
-1.00	-1.00	77.8930	77.8969	77.8967	77.8981	77.8949	77.8975
0.00	0.00	77.9000	77.9025	77.8971	77.9028	77.8986	77.9027
1.00	1.00	77.8994	77.9021	77.8944	77.8973	77.8969	77.8997
2.00	2.00	77.8967	77.8999	77.8986	77.8978	77.8977	77.8989
3.00	3.00	77.8977	77.9014	77.8991	77.8928	77.8984	77.8971
4.00	3.88	77.8866	77.8968	77.9183	77.8982	77.9025	77.8975
5.00	4.51	77.8570	77.8906	77.9430	77.9047	77.9000	77.8977
6.00	4.86	77.8212	77.8747	77.9852	77.9120	77.9032	77.8934
Average of averages						77.9002	77.8977
Standard deviation						0.0032	0.0023

## Results

The TG6 test component comprises a 200mm × 150mm × 12mm rectangular base plate made from Inconel 600 with three passes of Alloy 82 weld metal deposited in a slot of length 76mm. This not only has large grain issues in the weld region but a large interplanar spacing variation due to high strain gradients and a change in material composition. Each position was measured on E3 in steps of 1 degree, -3,-2-1,0,2,3° about the scattering vector and the value was then averaged. This was to reduce grain size effects [7]. Figure 2 shows the measurement of longitudinal direction (which is made in transmission geometry) along the central line of the TG6 specimen (denoted the BD line) using a 2×2×2 mm<sup>3</sup> gauge volume. This is the third measurement of the BD line on E3 (July 2017). The bulge at the back of the weld was set to y=12mm. The back plate surfaces immediately to the sides of the bulge were y=11.5mm. The total length of the BD line is 14.59 mm. The reference pin (denoted pin 3) is actually 14.36 mm, one surface however should correspond to the back face of the weld, i.e. the surface of the bulge at y=12mm. The bottom of the weld is at about y=5mm, where the parent material is from y=5 to 12mm.

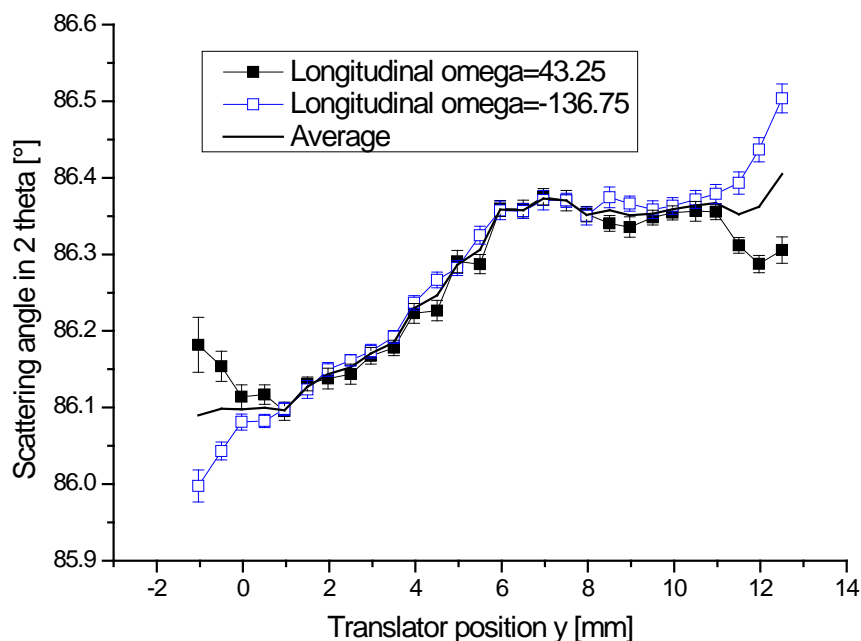


Figure 2. Measurement of the longitudinal direction along the BD line in the TG6 specimen.

The figure shows that there is indeed the surface effect as the gauge volume exits the surface. The coincidence of the lines where the gauge volume is fully submersed proves the good alignment of the primary slit over the centre of rotation of the diffractometer's omega table. The measurement was made in transmission geometry. Conversely the normal direction was measured in reflection geometry. This is susceptible to an absorption effect [6] which can be clearly seen in figure 3. This is because the centre of gravity of the gauge volume in terms of scattered neutrons in reflection geometry is at slightly different position to the geometrical centre of the gauge volume. Measurement however is difficult on E3 over the complete BD line from one side as the neutron absorption of the nickel alloy is very high. Taking an average of the

values where there are two values gives the correct value for the position [6]. It is advised that the region where one can do overlapping measurements is measured first so one can find the absorption shift, so one can work out the translator positions that correspond to the intended measurement positions.

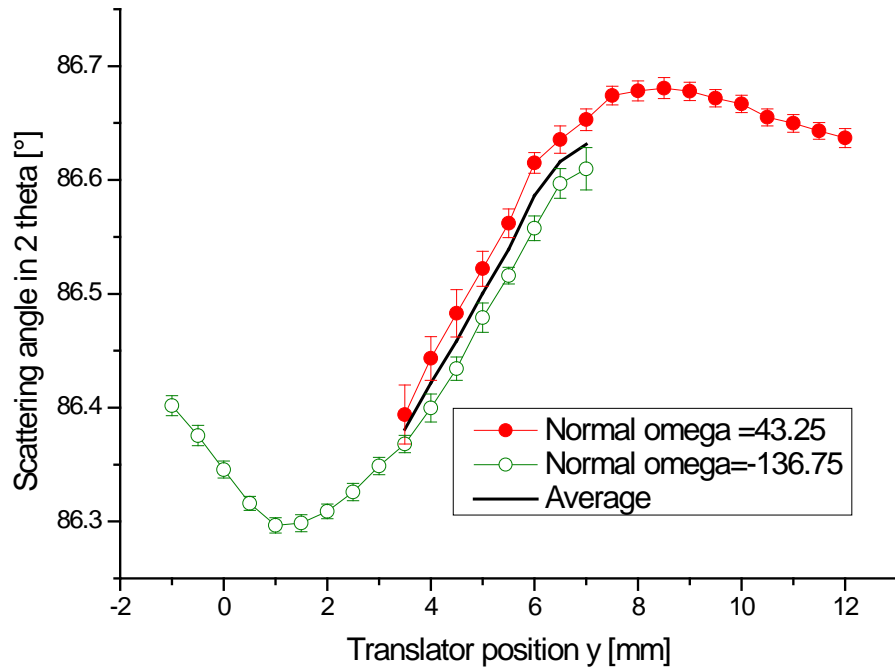


Figure 3. Measurement of normal direction along the BD line in the TG6 specimen on E3.

A 5mm slice of the weld was also available which turned out to be better for relative positioning of corresponding reference values for the welded plate compared to the pin (see figure 4). The stress is much smaller in the slice compared to the plate. Two plane stress calculations were made in the slice (assuming the longitudinal stress and normal stress directions were zero respectively) and these agree with each other well. For a comparison, the reference value needed to set the normal direction =0MPa in the welded plate is also depicted and this agrees with the slice positioning. One can fit the distribution with a Sigmoidal function and the centre position of the three values obtain agrees to within  $4.87 \pm 0.06$ mm. There is a slight offset with respect with the reference pin which was  $4.56 \pm 0.04$  mm. This corresponds to the difference in length of the pin (14.36 mm) and the actual length of the BD line (14.59 mm) to within experimental uncertainty.

Final stress calculations agree mostly very well with measurements made on Stress-Spec [8] at the FRMII (see figure 5). The normal strain was also made using the ‘180°’ technique but one was able to measure along the whole BD line due to the higher flux at FRMII and so the average values were made across the whole of the BD line. Agreement of the normal stress in the weld near the surface is not so good; this may be due to grain size issues that were not canceled out due to normal strain not being completely measured from both sides on E3. The best agreement is in the parent region where the grain size is smaller. The normal stress at the surface is 0 MPa

as expected. A value of near 0 MPa was also obtained on the Stress-Spec measurement in the weld region.

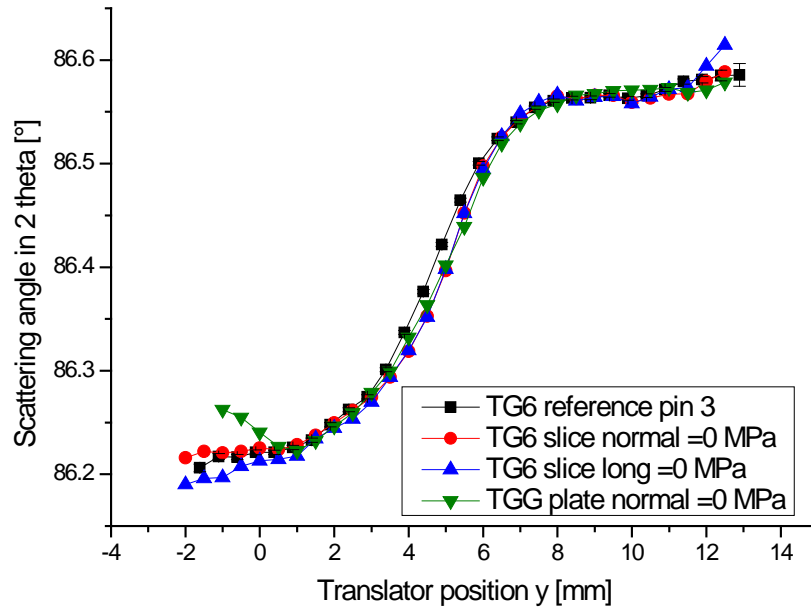


Figure 4. Comparison of reference values obtained from the TG6 pin, slice and plate.

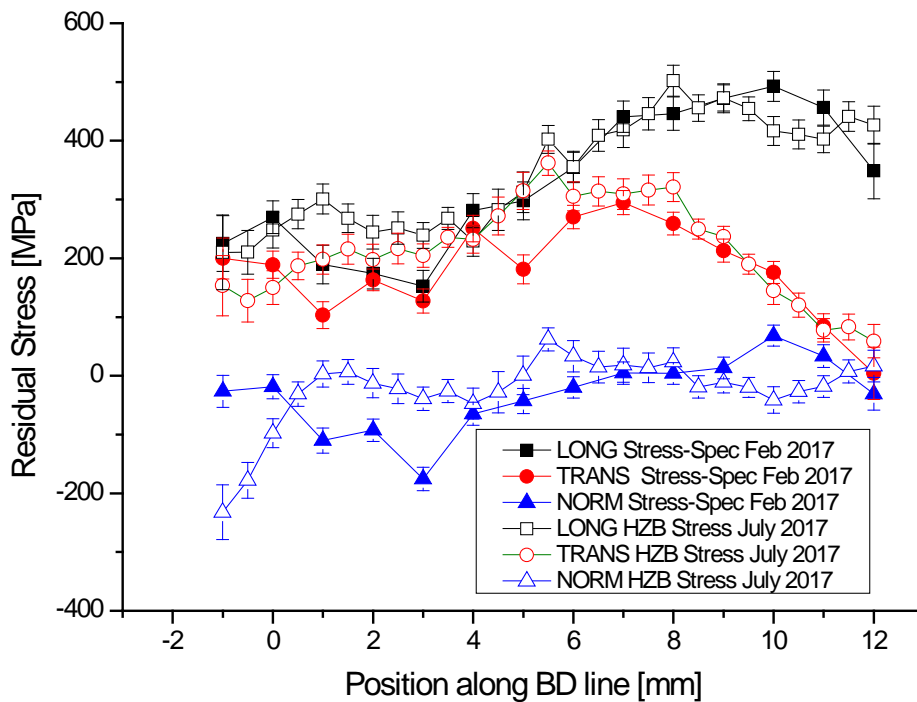


Figure 5. Comparison of stress from Stress-Spec and E3 at the HZB along the BD plate line.

## Summary

The Net TG6 round robin specimen presented itself to be a challenge when determining the strain and stress using neutrons. Measuring the normal strain can be difficult when there is a large neutron path length and getting a complete overlap of measurements is challenging when using the 180° technique. Agreement of the normal stress in the two measurements presented in the weld near the surface is not so good; this may be due to grain size issues that were not canceled out due to normal strain not being completely measured from both sides on E3. The best agreement is in the parent region where the grain size is smaller. The normal stress at the surface is 0 MPa as expected. A value of near 0 MPa was also obtained on the Stress-Spec measurement in the weld region. In general using the 180° technique is useful for measuring near surfaces to get a more accurate value of strain. This technique also cancels out the absorption effect [6] and also can be used for grain size effect mitigation [5]. The sample has a large interplanar spacing variation due to high strain gradients and a change in material composition. The gradients due to only the material composition can be seen in figure 4. A Sigmoidal function can be used to fit these reference distributions to obtain a better positioning to obtain accurate strain values in the welded plate.

## References

- [1] Webster, P.J., Mills, G., Wang, X.D., Kang, W.P., Holden, T.M. 'Impediments to Efficient Through-Surface Strain Scanning', *Journal of Neutron Research*, vol. 3, no. 4, pp. 223-240, 1996. <https://doi.org/10.1080/10238169608200197>
- [2] M. Vrána and P. Mikula, "Suppression of Surface Effect by Using Bent-Perfect-Crystal Monochromator in Residual Strain Scanning", *Materials Science Forum*, Vols. 490-491, pp. 234-238, 2005. <https://doi.org/10.4028/www.scientific.net/MSF.490-491.234>
- [3] Saroun, J., Kornmeier, J. R., Hofmann, M., Mikula, P. & Vrána, M. (2013). *J. Appl. Cryst.* 46, 628-638. <https://doi.org/10.1107/S0021889813008194>
- [4] Wimpory, R. C., Mikula, P., Šaroun, J., Poeste, T., Li, J., Hofmann, M. and Schneider, R. *Neutron News*, 19, (2008), 16 - 19. <https://doi.org/10.1080/10448630701831995>
- [5] Holden, T. M., Traore, Y., James, J., Kelleher, J. & Bouchard, P. J. (2015). *J. Appl. Cryst.* 48, 582-584. <https://doi.org/10.1107/S1600576715002757>
- [6] "Precise measurement of steep residual strain gradients using neutron diffraction in strongly absorbing materials with chemical compositional gradients", Robert C. Wimpory, Michael Hofmann, Vasileios Akrivos, Mike C Smith, Thilo Pirling and Carsten Ohms., Accepted for publication in *Materials Performance and Characterization* 2018
- [7] Robert Charles Wimpory, René V. Martins, Michael Hofmann, Joana Rebelo Kornmeier, Shanmukha Moturu, Carsten Ohms, *International Journal of Pressure Vessels and Piping*, 2017, ISSN 0308-0161. <https://doi.org/10.1016/j.ijpvp.2017.09.002>
- [8] Hofmann, M., Schneider, R., Seidl, G.A., Kornmeier, J., Wimpory, R., Garbe, U. und Brokmeier, H.G., *Physica B*, 2006, 385 – 368, 1035 - 1037

# Neutron Strain Scanning of Duplex Steel Subjected to 4-Point-Bending with Particular Regard to the Strain Free Lattice Parameter $D_0$

S. Pulvermacher<sup>1,a</sup>, J. Gibmeier<sup>1,b</sup>, J. Saroun<sup>2,c</sup>, J. Rebelo Kornmeier<sup>3,d</sup>,  
F. Vollert<sup>1,e</sup> and T. Pirling<sup>4,f</sup>

<sup>1</sup>Karlsruher Institut für Technologie, IAM-WK, Kaiserstraße 12, 76131 Karlsruhe, Germany

<sup>2</sup>Nuclear Physics Institute of the ASCR, 250 68 Řež, Czech Republic

<sup>3</sup>Heinz Maier-Leibnitz Zentrum (MLZ), TU München, D-85748 Garching, Germany

<sup>4</sup>Institut Laue-Langevin, 38042 Grenoble, France

<sup>a</sup>[samuel.pulvermacher@kit.edu](mailto:samuel.pulvermacher@kit.edu), <sup>b</sup>[jens.gibmeier@kit.edu](mailto:jens.gibmeier@kit.edu), <sup>c</sup>[saroun@ujf.cas.cz](mailto:saroun@ujf.cas.cz),

<sup>d</sup>[joana.kornmeier@frm2.tum.de](mailto:joana.kornmeier@frm2.tum.de), <sup>e</sup>[florian.vollert@kit.edu](mailto:florian.vollert@kit.edu), <sup>f</sup>[pirling@ill.eu](mailto:pirling@ill.eu)

**Keywords:** Neutron Strain Scanning, Phase Specific Strain, 4-Point Bending, Stress Free Lattice Parameter, Duplex Steel

**Abstract.** Neutronographic residual stress analysis on multiphase materials is challenging with regard to phase-specific micro residual stresses and to the consideration of an appropriate stress free lattice parameter for meaningful lattice strain calculation. Even in case of randomly textured materials stress analysis becomes more elaborate due to plastic anisotropy effects. According to literature for stress analysis using neutron diffraction lattice planes should be chosen that are less prone to plastic anisotropy. These are the  $\{311\}$  austenite and the  $\{220\}$  ferrite planes in case of duplex steels. Here, we report about phase-specific in-situ neutron strain scanning at SALSA@ILL, Grenoble during defined 4-point-bending of duplex steel X2CrNiMoN22-5-3 using exactly these two recommended diffraction lines. It is shown that due to the local texture of the bending bars, which was cut from a hot rolled cylindrical rod, strong plastic anisotropy was determined. This effect must be taken into account for diffraction based residual stress analysis to prevent from erroneous stress determination.

## Introduction

For non-destructive residual stress analysis for the inside of technical components beside high energy synchrotron X-ray diffraction, neutron diffraction is often the method of choice. In this regard a meaningful measure of the stress / strain free or stress / strain independent lattice parameter  $D_0$  is required for calculating lattice strains from the determined interplanar lattice spacings. Different procedures are explained how to provide appropriate data for  $D_0$  as e.g. determining the interplanar lattice spacings for the 'stress free state' in an area with negligible (residual) stress or to cut cubes or comb structures out of the material, which in turn leads to a partial and adequate stress release [1]. In case of multi-phase materials, phase specific micro residual stresses can impede these well established procedures since it is questionable if the micro residual stresses will be released during cutting the samples. Assuming that the macro residual stresses are sufficiently released significant phase specific residual stresses might remain and will in consequence affect the local stress free lattice parameter.

For diffraction stress analysis in multiphase materials it is recommended to determine phase specific lattice strains in all phases if the phase content exceeds a volume share of about 10%. By this means macro (residual) stresses can be determined using a rule of mixture and the volume share of the contributing phases as weighting factor. Duplex steels represent typical applicants in



this field. Here, large amount of austenite phase coexists with ferrite, hence for this gross two-phase material neutronographic stress/strain analysis strongly requires consideration of both phases and thus also the determination of appropriate phase specific stress free lattice parameters  $D_{0,\alpha}$  and  $D_{0,\gamma}$ . For the assessment of manufacturing processes by means of process induced residual stresses often the separation of macro and micro residual stresses and in this regard the load partitioning on the two phases is of special interest. In this context in [2] the phase specific lattice strains for various  $\{hkl\}$  lattice planes for duplex steel subjected to defined macroscopic elastic and elasto-plastic uniaxial loading were studied using neutron diffraction. It has been shown that apart of the elastic anisotropy plastic anisotropy effects occur due to the fact that crystallites do not deform homogeneously since the deformation depends on the slip systems. Regarding the load partitioning for different lattice planes this plastic anisotropy in part strongly deviates from the elastic behavior. For practical applications the authors recommended to consider only lattice planes for (residual) stress analysis which have no or only a weak anisotropic effect. In accordance with [3,4] for fcc materials the  $\{111\}$ ,  $\{311\}$  and  $\{422\}$  planes and for bcc materials the  $\{110\}$  or  $\{211\}$  planes are less prone to plastic anisotropy effects. In preliminary studies on load partitioning in duplex steels we noticed that crystallographic texture might have a strong impact on the plastic anisotropy. However, crystallographic texture was not discussed in the above mentioned works. The knowledge about the impact of crystallographic texture on plastic anisotropy is essential for the planning, the evaluation and assessment of neutronographic stress analysis, not least since semi-finished parts or technical components made of duplex steels often exhibit characteristic textures due to the processing route. To study the effect of texture on the load partitioning behavior for this first approach rectangular shapes bars were extracted from cylindrical rods of duplex steel X2CrNiMoN22-5-3 exhibiting phase fractions of about 50% ferrite ( $\alpha$ ) and 50% austenite ( $\gamma$ ). For samples subjected to defined 4-point-bending using purely elastic and elasto-plastic loading neutronographic strain scanning in both phases was carried out with respect to the coordinate of the bending height on instrument SALSA@ILL, Grenoble. 4-point-bending experiments have the charm that within a single experiment different uniaxial loading states can be studied for different location at the bar. Considering purely elastic and elasto-plastic loading allows for the separation between elastic and plastic anisotropy effects. To provide meaningful data for the phase specific stress free lattice parameters  $D_{0,\{hkl\}}$  the locally existing lattice parameters of the sample prior to the loading experiment is determined and applied for local lattice strain calculation.

#### Material and experimental Procedures:

The used material is a hot-rolled duplex steel X2CrNiMoN22-5-3 (mat.no. 1.4462) with a diameter of 30 mm exhibiting a ferrite to austenite ratio of approximately 50:50. The microstructure is shown in Fig. 1 for a cut in longitudinal direction. Metallographic analysis revealed an average grain size in rolling direction (later longitudinal direction) of approx. 74  $\mu\text{m}$ , 6  $\mu\text{m}$  in transverse direction and 5  $\mu\text{m}$  in normal direction, respectively. The sample geometry is 160 x 15 x 10 mm. Figure 2 shows a schematic view of the sample with the assigned coordinate system together with indication of the applied 4-point-bending loading.

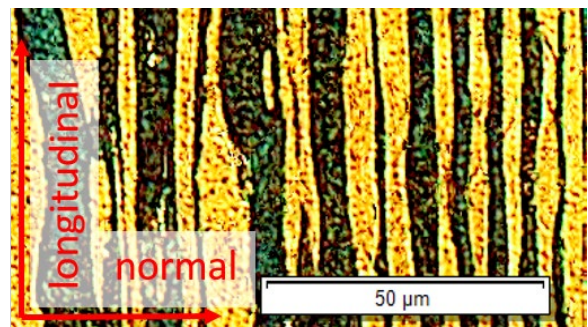


Figure 1: Microstructure of the duplex steel for a section from a cut in longitudinal direction of the used bars, etchant: Behara II, bright regions: austenite, dark regions: ferrite

In the as received state the duplex steel was de facto stress free as verified by means of hole drilling and X-ray stress analysis. As indicated in the introduction part the bars exhibit a rather strong crystallographic texture in both phases with a gradient over the bending height. Since the bending bars were not exactly cut from the centre of the as delivered steel rod the texture distribution is not symmetric to the mid layer of the bars. Fig. 3 shows as an example the texture distribution for the later compressive loaded layer, the mid layer and for the later tensile loaded layer for both phases for the  $\phi 2 = 45^\circ$  sections of the ODF (orientation distribution function) determined by means of X-ray diffraction prior to the neutron diffraction experiment. In total the ODF was determined for 10 locations distributed over the bending height. The ODF cuts exemplarily shown in Fig. 3

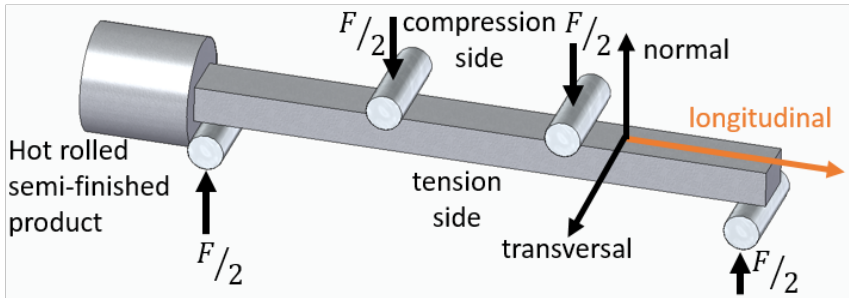


Figure 2: Schematic sketch of the bending bar with indication of the applied coordinate system

clearly indicate that (a) a gradient in the crystallographic texture exist in both phases and (b) that the sharpness of the texture is much higher in case of the ferrite phase (in particular on the later compressive loaded side).

Neutron strain scanning with respect to the bending height was carried out in all three principal directions, i.e. in longitudinal, transverse and normal direction (see Fig 2) in both phases for various  $\{hkl\}$  planes at the SALSA experiment at ILL [5], Grenoble using a wavelength of 1.6 Å. A nominal gauge volume of  $0.6 \times 0.6 \times 10$  mm was defined by radial collimators at the primary and secondary beam paths; the 10 mm axis was always parallel to the longitudinal direction of the bar. In total two ferrite ( $\alpha$ -Fe) lattice planes ( $\{211\}$ ,  $\{220\}$ ) and three austenite ( $\gamma$ -Fe) lattice planes ( $\{220\}$ ,  $\{222\}$ ,  $\{311\}$ ) were measured separately. Due to the rather strong local texture not for all directions interference lines could be recorded with intensities being sufficient for meaningful evaluation of the line positions. That means that the local texture impeded stress determination at all. Here, we only focus on the  $\{220\}$   $\alpha$ -ferrite and on the  $\{311\}$  austenite lattice planes, which are (according to literature) expected to be less prone to plastic anisotropy. Furthermore, we only focus on the strain scanning of the longitudinal component, which corresponds to the loading direction, to study the load partitioning in both phases. The peak fitting was realized using a Gaussian function subsequent to background subtraction. Only measurement locations, where the entire nominal gauge volume is immersed into material are considered. The phase specific values of the stress free lattice parameters  $D_{0,\{hkl\}}$  were determined on the bending bar prior to the bending loading at the same positions, which were used for later in-situ lattice strain scanning during loading. Since, the  $D_0$  scanning was carried out for less measuring points as in case of the in-situ experiments linear interpolation was applied. For in-situ neutron strain scanning during defined bending loading two different load stages were considered: (i) purely elastically deformed (0.22% total strain) and (ii) elasto-plastically deformed (approx. 1.5 % total strain). The loading was controlled via the total strain measured by strain gauges at both outer fibres of the bar. The loading stress were assigned using a reference bending stress-strain curve determined on an instrumented universal testing machine prior to the neutron beamtime using the same support distances as given by the 4-point bending device applied at SALSA (see Fig. 2).

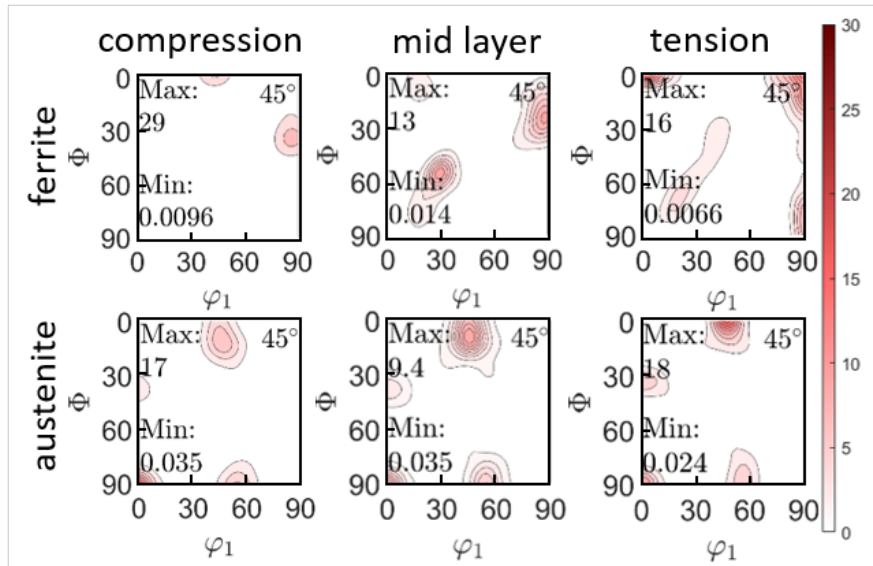


Figure 3:  $\phi_2 = 45^\circ$  sections of the ODF determined by means of X-ray diffraction for three selected positions of the bending bar.

### Experimental results and discussion

Figures 4 (A) and (B) show the interplanar lattice spacings for the initial state of the bending bar determined for the  $\{311\}$   $\gamma$ -Fe and the  $\{220\}$   $\alpha$ -Fe lattice planes, respectively. The data indicate that the stress free lattice parameters  $D_{0,\{hkl\}}$  shows a characteristic distribution presumable due to the processing route (hot rolling) of the rods, which leads to local texture and the generation of phase specific micro residual stresses. On the side with negative coordinates (later compressive loaded side) large errors bars result for the ferrite phase, which is due to local texture distribution and the connected weak intensities of the  $\{220\}$  interference lines. Regarding lattice strains that can be assigned to the changes in lattice parameters  $D_0$ , these changes in lattice parameters correspond to rather high strain (up to about 0.0016). Hence, neglecting this initial state might result in erroneous stress data. Consequently, the lattice strains presented in Fig. 4 (C) for the purely elastic case ( $\epsilon_t = 0.22\%$ ) and Fig. 5 (A) for the elasto-plastic case ( $\epsilon_t = 1.5\%$ ) are lattice strain differences  $\Delta\epsilon$  calculated with reference to this initial state.

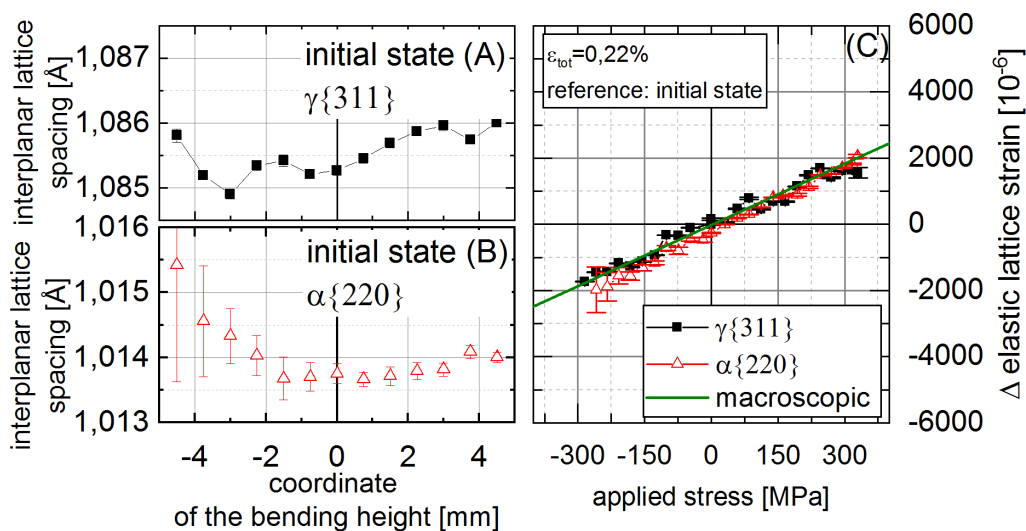


Figure 4: Phase-specific interplanar lattice spacings determined for the in the initial state of the bending bar for (A) the  $\{311\}$  austenite lines and (B) for the  $\{220\}$  ferrite lines. In (C) the change in lattice strains  $\Delta\epsilon$  with respect to the initial state for the macroscopically purely elastic loading state is shown. For better orientation the macroscopic  $\epsilon$  vs.  $\sigma$  distribution is plotted.

In Fig. 4 (C) the lattice strain difference  $\Delta\varepsilon$  for the purely elastic loading vs. the applied stress is shown. For the  $\{311\}$   $\gamma$ -Fe and the  $\{220\}$   $\alpha$ -Fe lattice planes almost linear courses are determined. Furthermore, both distributions roughly follow the macroscopic distribution, which can be expected for the orientation factors of  $3\Gamma = 0.471$  for the  $\{311\}$  austenite and  $3\Gamma = 0.75$  for the  $\{220\}$  ferrite planes. Both values are close to  $3\Gamma = 0.6$ , which generally reflects the macroscopic behavior.

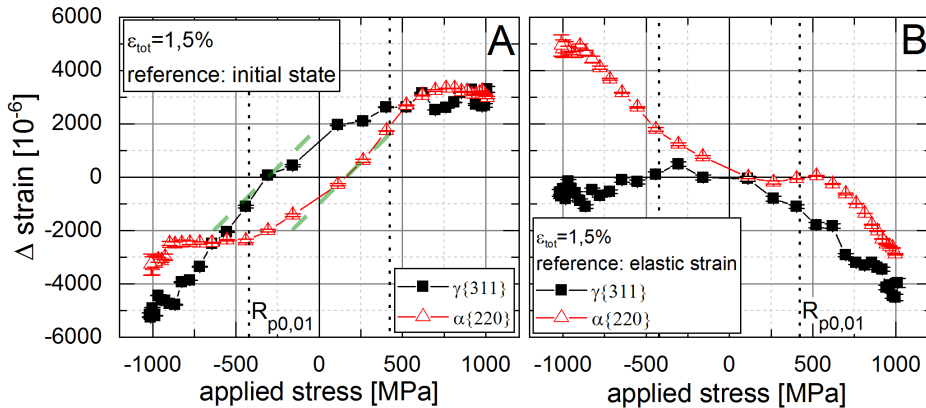


Figure 5: (A) change in phase-specific lattice strains  $\Delta\varepsilon$  with respect to the initial state for elasto-plastic loading to  $\varepsilon_t = 1.5\%$ . For better orientation the macroscopic 0.01% proof stress  $R_{p0.01}$  is added to the plot; (B) change in phase-specific lattice strains  $\Delta\varepsilon$  after subtraction of the fictitious elastic materials response for the same loading state.

In Fig. 5 (B) the phase-specific load partitioning for the duplex steel in case of elasto-plastic loading is displayed for the loading with total strains in the outer layers of the bending bar of approx. 1.5%. Again the change in lattice strain with reference to the initial state is presented. In Fig. 5 (B) the same data is plotted as used in Fig. 5 (A), but here the fictitious elastic strain is subtracted for both phases using the trend determined for the purely elastic loading as shown in Fig. 4 (C). Here, the zero passage determined in Fig. 5 (A) is maintained for both phases. By this means the change in phase specific lattice strain plotted in Fig. 5 (B) indicate, when the individual phases start to plastify and by this means, differences in the phase specific materials response can be noticed more conveniently. To provide better orientation the 0.01% proof stress  $R_{p0.01}$  (423 MPa) as determined by the macroscopic bending work hardening curve is added. The changes in phase specific lattice strains with respect to the initial state (Fig. 5(A)) indicate that in both phases large deviations to the behavior expected based on the work of [2] occur. In particular for the  $\{220\}$   $\alpha$ -Fe interference line it is expected that no significant plastic anisotropy exists. However, for both phases strong plastic anisotropy effects occur, which can be explained by the phase-specific texture exhibiting a strong gradient through the bending bar (see Fig. 3). According to [2] the strain response for the  $\{220\}$  ferrite lattice planes should follow the trend from the elastic regime. However, in the present case on both sides, i.e. the tensile and the compressive loaded side strong deviations occur, indicating that local phase-specific plastic deformation is strongly affected by the local crystallographic texture. That means that the texture is such that crystallites deform inhomogenously over the cross section of the bars. The reason is that the crystallites are orientated such that slip planes and slip directions are oriented in a way that dislocation gliding during bending loading is promoted in contrast to a more random orientation. In detail this will be studied by means of simulation based on crystal plasticity modelling taking into account the local gradient in crystallographic texture and is part of current research efforts. Here, the results of neutronographic strain scanning will be used for validation of the modelling approach.

A closer look to the data plotted in Fig. 5 (A) further reveals that the observed behavior is asymmetric when comparing the compressive with the tensile loaded side. The asymmetric phase-specific plastic deformation obviously causes a shift of the neutral fiber in both phases, i.e. in ferrite slightly towards the tensile and in austenite slightly towards the compressive loaded side. Obviously, the neutral fiber resulting for the macroscopic behavior is slightly shifted towards the compressive loaded side under consideration of the volume content, which is about 50:50. This shift of the neutral fiber (characterizing the macroscopic behavior) is nothing odd and can also be explained by means of the texture gradient.

The change in phase specific lattice strains when subtracting the fictitious elastic response supports the above mentioned statements. From this plot it can be clearly derived that for the  $\{220\}$  ferrite line a very pronounced plastic anisotropy in tension and in compression can be noticed, while on the tensile loaded side the slope appears to be slightly steeper. In contrast, strong plastic anisotropy can be observed for the  $\{311\}$  austenite interference line. On the compressive loaded side the local texture causes that almost no plastic anisotropy occurs. The local crystallographic texture induces a phase specific mechanical response that strongly deviates from literature. Hence, following the recommendations for consideration of the  $\{311\}$  austenite and the  $\{220\}$  ferrite interference lines will definitely result in erroneous phase specific residual stresses, when the effect of local crystallographic texture on the plastic deformation behavior is unattended during data evaluation and assessment. Hence, in case that texture is expected from the processing route, special care must be taken in regard to phase-specific plastic anisotropy.

### Summary

In-situ neutronographic phase specific strain scanning during elastic and elasto-plastic 4-point bending was performed for duplex steel X2CrNiMoN22-5-3. The strain in load direction was determined for the  $\gamma\{311\}$  and the  $\alpha\{220\}$  interference lines under consideration of the local initial state of the bending bars prior to plastic deformation as  $D_0$  reference. Inconsistent with literature strong plastic anisotropy occurs for both interference lines, while a neglectable effect was expected. However, in literature local texture was not particularly taken into account. In the present case, local crystallographic texture cause this strong plastic anisotropy for interference lines, which are often recommended and applied for local neutron stress analysis. Based on the findings special care on the texture induced plastic anisotropy must be taken for data evaluation and assessment for duplex steels, which often show pronounced texture induced by processing.

### Acknowledgements

The work was partly supported through a joint project funded by the Czech Science Foundation (project No. 16-08803J) and the German Research Foundation (DFG project GI 376/11-1 and HO 3322/4-1) and by the Czech Ministry of Education, Youth and Sports (project no. LM2015050). The authors are grateful for granting beamtime at ILL (proposal No. 1-02-199).

### References

- [1] Withers, P. J., Preuss M., Steuwer A., Pang J. W. L., Appl. Crystallogr. 40 (2007), pp. 891–904. <https://doi.org/10.1107/S0021889807030269>
- [2] Allen, A. J.; Bourke, M.; David, W. I. F.; Dawes, S.; Hutchings, M. T.; Krawitz, A. D.; Windsor, C. G., ICRS 1989, pp. 78-83
- [3] Clausen B., Lorentzen T., Bourke M., Daymond M., Mat. Sci. Eng. A, 259 (1999), pp. 17-24. [https://doi.org/10.1016/S0921-5093\(98\)00878-8](https://doi.org/10.1016/S0921-5093(98)00878-8)
- [4] Pang, J.W.L; Holden, T.M; Mason, T.E., Acta Mat., (1998), pp. 1503-1518. [https://doi.org/10.1016/S1359-6454\(97\)00369-8](https://doi.org/10.1016/S1359-6454(97)00369-8)
- [5] Pirling, T. Bruno, G., Withers, P., Mat. Sci. Eng. A, 437 (2006), pp. 139-144. <https://doi.org/10.1016/j.msea.2006.04.083>



# Plastic Deformation of InSb Micro-Pillars: A Comparative Study Between Spatially Resolved Laue and Monochromatic X-Ray Micro-Diffraction Maps

Tarik Sadat<sup>1,a,\*</sup>, Mariana Verezhak<sup>2,b</sup>, Pierre Godard<sup>1,c</sup>, Pierre Olivier Renault<sup>1,d</sup>, Steven Van Petegem<sup>2,e</sup>, Vincent Jacques<sup>3,f</sup>, Ana Diaz<sup>2,g</sup>, Daniel Grolimund<sup>2,h</sup>, Ludovic Thilly<sup>1,i</sup>

<sup>1</sup>Institut Pprime, CNRS, Université de Poitiers, SP2MI, Futuroscope Chasseneuil, France

<sup>2</sup>Paul Scherrer Institut, CH-5232 Villigen PSI, Switzerland

<sup>3</sup>Lab. Physique des Solides, CNRS, Université Paris-Sud, Orsay, France

<sup>a</sup>tarik.sadat@univ-poitiers.fr, <sup>b</sup>mariana.verezhak@psi.ch, <sup>c</sup>pierre.godard@univ-poitiers.fr, <sup>d</sup>pierre.olivier.renault@univ-poitiers.fr, <sup>e</sup>steven.vanpetegem@psi.ch, <sup>f</sup>vincent.jacques@u-psud.fr, <sup>g</sup>ana.diaz@psi.ch, <sup>h</sup>daniel.grolimund@psi.ch, <sup>i</sup>ludovic.thilly@univ-poitiers.fr

**Keywords:** Micro-Pillars, InSb, Laue Microdiffraction, Monochromatic Microdiffraction, Synchrotron Radiation, Plasticity

**Abstract.** Indium Antimonide (InSb) single-crystalline micro-pillars were mechanically deformed by uniaxial compression loading-unloading cycles up to the beginning of the plastic regime. After deformation, 2D spatially resolved maps were collected via two X-Ray Diffraction (XRD) techniques: polychromatic micro-Laue and monochromatic micro-diffraction. In both techniques, the integrated diffracted intensity shows strong variations inside the pillar. Moreover, the shift and streaking of one spot in polychromatic XRD as well as the lattice strain and tilt components derived from monochromatic XRD reveal that the plastically deformed area is localized on the top of the pillar, in agreement with scanning electron microscopy images. The two XRD techniques are thus providing correlated but yet complementary information.

## Introduction

Indium Antimonide (InSb) and other semiconductors are known to be crystalline materials with brittle behavior at room temperature in the bulk state, but become ductile in the form of micro- and nano-objects [1-2]. At room temperature, InSb micro-pillars plastically deform by the nucleation of partial dislocations at surfaces: after gliding through the pillar, they escape at opposite surfaces (creating slip traces forming a deformation band) but leave in the crystal parallel Stacking Faults (SFs). This mechanism has been verified by post-mortem Scanning Electron Microscopy (SEM) observations and destructive Transmission Electron Microscopy (TEM) characterization [1-2] but also by non-destructive post-mortem study based on coherent X-Ray diffraction [3]. In the latter case, the profile of coherent diffraction patterns of 202 reflection evolves significantly between pristine and plastically-deformed regions: the splitting and streaking of patterns arise from interferences induced by the presence of SFs that are phase-defects creating phase-shifted regions within the pillar [3]. The maximum intensity of diffraction patterns could be related to the number of SFs present in the illuminated volume, and also to the volume of defected region (i.e. the size of the band containing the SFs). This diffraction technique thus proved to be very interesting as a non-destructive way to detect and characterize the presence of plastic defects in nano- and micro-objects.

